Published in final edited form as:
J Biomed Opt. 2009 ; 14(3): 034018. doi:10.1117/1.3147407.

Single-walled carbon nanotubes as a multimodal — thermoacoustic and photoacoustic — contrast agent

Manojit Pramanik[1,*], **Magdalena Swierczewska**[2,†], **Danielle Green**[2,‡], **Balaji Sitharaman**[2,§], and **Lihong V. Wang**[1,**]

[1] Optical Imaging Laboratory, Department of Biomedical Engineering, Washington University in St. Louis, Campus Box 1097, One Brookings Drive, St. Louis, MO 63130, USA

[2] Department of Biomedical Engineering, State University of New York at Stony Brook, Stony Brook, New York 11794, USA

Abstract

We have developed a novel carbon nanotube-based contrast agent for both thermoacoustic and photoacoustic tomography. In comparison with de-ionized water, single-walled carbon nanotubes exhibited more than two-fold signal enhancement for thermoacoustic tomography at 3 GHz. In comparison with blood, they exhibited more than six-fold signal enhancement for photoacoustic tomography at 1064 nm wavelength. The large contrast enhancement of single-walled carbon nanotubes was further corroborated by tissue phantom imaging studies.

Keywords

thermoacoustic tomography; photoacoustic tomography; contrast agents; single-walled carbon nanotubes; carbon nanotubes

Introduction

The advent of numerous noninvasive imaging modalities, such as X-ray, computed tomography (CT), single photon emission computed tomography (SPECT), positron emission tomography (PET), magnetic resonance imaging (MRI), ultrasound imaging (US), radio frequency (rf), and optical imaging now allows scientists and clinicians to acquire *in vivo* images of the anatomy and physiology of animals and humans.[1,2] Each of these *in vivo* imaging techniques possesses characteristic strengths and weaknesses. For each imaging modality, substantial attention has been devoted to developing contrast agents not only for improving the contrast of the acquired images, but also for molecular imaging targeting specific biomolecules, cell tracking, and gene expression.[3–6]

We have developed hybrid imaging modalities, such as thermoacoustic tomography (TAT) and photoacoustic tomography (PAT), for different applications[7–11] and combined these two imaging modalities into a single imaging system for early breast cancer detection.[12] Diagnosis of cancer in its early stages depends on the recognition of subtle changes in tissue properties, such as mechanical properties, optical absorption, and rf absorption. For example, changes in

§Corresponding author (Nanotubes): Email: balaji.sitharaman@stonybrook.edu, Tel: (631) 632 1810, Fax: (631) 632-8577.
*Email: mano@biomed.wustl.edu
†Email: mswiercz@ic.sunysb.edu
‡Email: Danielle.Green@sunysb.edu
**Corresponding author (Photoacoustics): Email: lhwang@biomed.wustl.edu, Tel: (314) 935-6152, Fax: (314) 935-7448

ion and water concentrations lead to changes in rf absorption. To detect these changes, non ionizing rf electromagnetic waves and visible/near infrared (NIR) light-based imaging modalities have generated particular interest over the last decade.[7–11,13–17] TAT/PAT synergizes the advantages of pure-ultrasound and pure-rf/optical imaging,[7,13] allowing both satisfactory spatial resolution and high soft-tissue contrast. For instance, PAT is a unique noninvasive technology for imaging and quantifying the levels of vascularization and oxygen saturation in tumors.[9–11,18,19] These features are associated with angiogenesis and hypoxia accompanying malignant tumors.[20,21] TAT/PAT is also capable of revealing information such as water/ion concentration, blood volume, and oxygenation of hemoglobin. Since these parameters can change during the early stages of cancer, TAT/PAT offers opportunities for early detection. However, even though high rf and optical contrast exists between well-developed malignant tumor tissue and normal human breast tissue, the contrast during very early stages of cancer may be insufficient. Thus, a targeted contrast agent could be greatly beneficial for early cancer diagnosis using TAT/PAT.

Recently, carbon nanotube-based contrast agents have shown promise for a variety of imaging techniques.[22–25] The strategies for development of these contrast agents have included encapsulation of medically relevant metal ions within their carbon sheath,[22] external functionalization of the carbon sheath with a variety of imaging agents,[23,24] and exploiting the intrinsic physical properties of the carbon nanotubes (CNTs).[25] In this work, we have explored the intrinsic optical[26,27] and rf[28] absorbing properties of single-walled carbon nanotubes (SWNTs) with the goal of developing them as multimodal contrast agents for simultaneous TAT and PAT.

Methods and Materials

TAT/PAT scanner

A combined TAT/PAT scanner[12] was used for all the experimental studies in this work. Images were collected with microwave excitation (TAT) and then with laser excitation (PAT). For TAT, a 3.0 GHz microwave source with a 0.5 μs pulse width and 100 Hz pulse repetition rate was the rf source. The pulse energy was estimated to be around 10 mJ (= 20 kW × 0.5 μs), falling within the IEEE safety standards.[29] PAT was done at 1064 nm wavelength. A Q-switched Nd:YAG laser with a 10 Hz pulse repetition rate, 6.5 ns (@1064 nm wavelength) laser pulse width, and 850 mJ maximal output energy was the light source. The incident laser fluence on the sample surface was controlled to be < 20 mJ/cm^2, conforming to the American National Standards Institute (ANSI) standards.[30] The generated acoustic signals were detected using two different nonfocused transducers operating at a 2.25 MHz central frequency (13-mm-diameter active area, ISS 2.25 × 0.5 COM; 6-mm-diameter active area, ISS 2.25 × 0.25 COM, Krautkramer). For cross-sectional TAT/PAT imaging, data was collected around the sample in a full circle. Different reconstruction algorithms can be used to reconstruct TAT/PAT images from raw data.[16] Here, a delay and sum (backprojection) algorithm was used for all image reconstruction.[16] The sample was placed inside the breast holder chamber, which was filled with mineral oil. Mineral oil does not absorb microwaves. Moreover, since mineral oil is transparent, the light absorption is also very small. Mineral oil also acts as a coupling medium for sound propagation. Thus for all our experiments mineral oil was an ideal choice as a background medium.

PA imaging system

A reflection-mode PA imaging system[31] was used to test the *in vitro* blood signal enhancement using the SWNTs. A tunable Ti:sapphire laser (LT-2211A, LOTIS TII) pumped by a Q-switched Nd:YAG (LS-2137, LOTIS II) laser was the light source, providing <15 ns pulse duration and a 10-Hz pulse repetition rate. A 5 MHz central frequency, spherically focused

ultrasonic transducer (V308, Panametrics-NDT) was used to acquire the generated PA signals. The transducer had a 2.54 cm focus length, a 1.91 cm diameter active area element, and 72% bandwidth. The signal was then amplified by a low-noise amplifier (5072PR, Panametrics-NDT), and recorded using a digital oscilloscope (TDS 5054, Tektronix) with a 50 mega-sampling rate. PA signal fluctuations due to pulse-to-pulse energy variation were compensated by signals from a photodiode (DET110, Thorlabs), which sampled the energy of each laser pulse.

SWNTs synthesis

A diblock copolymer templating method was used to coat Fe coated on Si wafers.[32] The wafers were placed in a 3 inch quartz reaction chamber (Easy Tube 2000, First Nano) and heated in Ar to 900°C. The chamber was filled with H_2 for 2 minutes and CH_4 was added to the gas flow as the carbon feedstock for 20 minutes to initiate the growth of SWNTs. Subsequently, the carbon feedstock was switched off and the furnace was cooled to room temperature. Raman spectroscopy (LabRAM Aramis, Horiba JvonYvon) at 633 nm excitation, transmission electron microscope (TEM) imaging (JEOL 2000 FX electron microscope operating at 200 kV), zeta potential (Malvern Zetasizer NanoZS system with irradiation from a 632.8 nm He-Ne laser), and atomic force microscopy (AFM MFD-3D-BIO, Asylum Research) were used to characterize the SWNTs.

Figure 1(a) shows a representative bright field transmission electron microscopy (TEM) image of densely populated SWNTs on the surface of the substrate. Further investigation by high resolution TEM (HRTEM) (Figure 1(b)) and atomic force microscopy (AFM) (Figure 1(c)) showed SWNTs with diameters between 1.2 and 2.2 nm and lengths between 500 nm and 1 μm. Figure 1(d) shows a representative Raman spectrum of SWNTs at the laser excitation wavelength of 633 nm. The Raman spectrum shows a G band at 1596 cm^{-1} and a D band at 1320 cm^{-1}, with a D/G band ratio for Gd-SWNTs less than 0.1, indicating that the SWNTs have very few defects.[33] The radial breathing modes (Fig. 1(d) inset), unique to SWNTs,[33] further corroborate the HRTEM and AFM results and confirm the presence of SWNTs. Four types of multi-walled carbon nanotubes (MWNTs) of various inner and outer diameters, fullerenes (Sigma-Aldrich, USA, catalog numbers: 483036), and graphite microparticles (Sigma-Aldrich, USA, catalog numbers: 496596) were also used for initial studies. SWNT suspensions with different concentrations (0.1–1 mg/ml) were prepared in 10 ml of 1% biologically compatible Pluronic® F127 surfactant solution (pH 7). The different domains of the non-ionic Pluronic® F127 likely wrapped themselves in energy minimized conformations around the nanotubes to solubilize the SWNTs by steric stabilization, producing nearly-neutral nanotube suspensions.[34] These suspensions were stable during the period of the entire study. Zeta potential measurements were performed on 0.1 mg/ml SWNTs dispersed in Pluronic® F-127, and showed a peak *Zeta*-potential of −14 mV with a Gaussian distribution (full width half maximum of the distribution = 10 mV). This value is similar to other reported zeta potential measurements on neutral stable SWNTs dispersed in Pluronic® F127.[34] Figure 1(e) shows an optical image of the SWNTs (0.1–1 mg/ml concentration) dispersed in Pluronic® F127 after aggressive sonication.

Results and Discussions

A low density polyethylene (LDPE) vial with an inner diameter of 6 mm and 1 cc volume was used as a sample holder for the entire study. The vial was filled with the sample and placed inside the TAT/PAT scanner. De-ionized (DI) water was used for thermoacoustic (TA) signal comparison, whereas blood was used for photoacoustic (PA) signal comparison. Water, ions are two well known sources of microwave absorbers in the human body, and they produce strong TA signals. Therefore, to show that a new material (in this case SWNTs) can function

as a contrast agent, we have to first show that that SWNTs are capable of generating TA signals comparable to or stronger than a known TA signal producer in the body. The rf contrast between malignant tumor tissue and normal human breast tissue is as high as 4:1.[35] The rf absorption of water compared to background human breast tissue is also on the order of 4:1. Thus, we compared the rf absorption of SWNTs with that of water. Similarly, blood is a dominant light absorber in the human body and produces strong PA signals. Therefore, to show that SWNTs can function as a contrast agent in PA, we have to first show that SWNTs are capable of generating PA signals comparable to or stronger than that of a known absorber in the body. Blood was thus an obvious choice for comparison here. For the tissue phantom imaging, porcine fat was used as the background medium mimicking the tissue; the sample holder (LDPE vial) was inserted in the center of a ~6 cm diameter porcine fat cylinder approximately 1.5 cm high. The vial was filled with different samples (DI water, SWNTs, and blood) and images were collected. The hole inside the porcine fat had a slightly larger diameter than the sample holder's outside diameter.

Figure 2(a) shows the TA signal generated from the sample holder (LDPE vial) filled with DI water and with mineral oil. As we can clearly see, there is no TA signal from the sample holder filled with mineral oil (red line, showing only the noise of the system, no TA signal was observed). Therefore, the LDPE vial does not generate any TA signal. Moreover, the LDPE vial we used is semi transparent white, and therefore it does not absorb enough light to produce any measurable PA signal. Nevertheless, we tested the LDPE vial filled with blood and mineral oil under 1064 nm wavelength light. Figure 2(b) shows the PA signal generated from the vial. It is clearly seen that vial filled with mineral oil does not produce any significant PA signal at 1064 nm compared to the signal generated from blood. Therefore, we conclude that the sample holder vial has no effect either in TA or in PA signal generation, and henceforth all signals observed are considered to be generated from the sample placed inside the vial. We also tested the 1% Pluronic® F127 surfactant solution and observed no significant TA/PA signals. Figure 2(c) shows the TA signal generated from the LDPE vial filled with 1% Pluronic® F127 surfactant solution and DI water, and there is no significant contribution from the surfactant solution. Figure 2(d) shows the PA signal generated from blood and 1% Pluronic® F127 surfactant solution. Clearly, there is no PA signal generated from 1% Pluronic® F127 surfactant solution. Therefore, any TA/PA signal contribution coming from the Pluronic® F127 will be ignored in all future discussion.

An initial assessment was made for all the carbon nanostructures (SWNTs, MWNTs, C_{60}, and graphite microparticles). Table 1 summarizes the peak-to-peak TA/PA signal amplitudes obtained from various samples with the two different diameter transducers. Among all the samples, only SWNTs showed a significant increase in TA signal compared to DI water and a significant increase in PA signal compared to rat blood. To avoid over-interpretation of the data presented in Table 1 it is important to mention here that the TA and PA signals generated from the MWNT are not directly proportional to the outer diameter. Other parameters, such as the inner diameter, nanotube length, and number of concentric nanotubes, may also affect the generated signal amplitudes. The only conclusion that can be drawn from Table 1 is that the single-walled carbon nanotube sample generates a photoacoustic and thermoacoustic signal stronger than that from blood, water, and other carbon nanostructures. The increases in TA and PA signals were shown by pristine SWNTs (mass of Fe is ~20% of total weight of SWNT sample) as well as purified SWNTs (mass of Fe is ~0.5–1% of the total weight of SWNT sample), clearly indicating that the observed effects were due to the SWNTs and not due to the presence of iron. Since only SWNTs showed a significant increase in both TA and PA signals, they were used for further studies.

Figure 3(a) displays the TA signals from an LDPE vial filled with DI water and another vial filled with 1 mg/ml SWNTs. The peak-to-peak TA signal amplitudes generated by DI water

and 1 mg/ml SWNTs are 42 ± 0.32 mV and 101 ± 0.24 mV, respectively. Figure 3(b) shows the peak-to-peak TA signal amplitude and fractional increase in TA signal versus the concentration of SWNTs. The largest standard deviation of the data points, measuring 0.92 mV, was observed at 0.75 mg/ml concentration SWNTs. The data shows an approximately linear relationship between the TA signal amplitude and the SWNTs' concentration. We observe a maximum of 140% increase in the peak-to-peak signal amplitude for 1 mg/ml SWNTs over DI water. Figure 3(c) displays the PA signals from LDPE vial filled with blood and with 1 mg/ml SWNTs. The peak-to-peak PA signal amplitudes generated by blood and 1 mg/ml SWNTs are 0.22 ± 0.002 V and 1.32 ± 0.009 V, respectively. Figure 3(d) shows the peak-to-peak PA signal amplitude and fractional increase in PA signal versus the concentration of SWNTs. The largest standard deviation of the data points, measuring 0.027 V, was again observed at 0.75 mg/ml concentration SWNTs. The data shows again an approximately linear relationship between the PA signal amplitude and the SWNTs' concentration. We observe a maximum 490% increase in the peak-to-peak signal for 1 mg/ml SWNTs over blood. *In vitro* tests were carried out with SWNTs (0.1 mg/ml) mixed with blood in different proportions, and then PA signals were recorded. Keeping in mind that in other applications NIR light (700–800 nm) would be used for *in vivo* deep tissue imaging, the light used here was of 754 nm wavelength in the reflection mode PA imaging system[31]. A tube (Silastic® laboratory tubing, Dow Corning Corp., with I.D. 300 μm, O.D. 640 μm) was filled with blood, blood (90% v/v) + SWNTs (10% v/v), blood (75% v/v) + SWNTs (25% v/v), blood (50% v/v) + SWNTs (50% v/v), blood (25% v/v) + SWNTs (75% v/v), and SWNTs alone. Figure 3(e) shows the peak-to-peak PA signal amplitudes for those six samples, clearly indicating that the PA signal from blood was enhanced when SWNTs were mixed with the blood. The experiments were carried out 10 times to get the average and the standard deviation. We observed a PA signal of 1.37 ± 0.09 V from a mixture of 75% SWNTs and 25% blood, compared to a 0.44 ± 0.02 V PA signal from blood only. Therefore, when SWNTs were mixed with the blood, we saw a more than 210% increase in the PA signal at 754 nm wavelength.

Next, LDPE vials filled with different SWNTs samples were imaged in two dimensions using TAT and PAT. Figures 4(a) and 4(b) show the TAT cross sectional image of vial filled with DI water and SWNTs, respectively, clearly demonstrating a substantial improvement in the TA signal for the vial filled with SWNTs (both figures are shown in the same range of colorbar). Figures 4(c) and 4(d) compare the image profiles along the horizontal and vertical lines (dotted lines in Figs. 4(a) and 4(b)), respectively. Compared with DI water, SWNTs showed ~1.9 times and ~2.1 times signal improvements in the TA image along the horizontal and vertical lines, respectively (normalized to DI water). These results are consistent with the TA data presented in figure 3. Figures 4(e) and 4(f) show cross sectional PAT images of the vial filled with blood and SWNTs, respectively, showing an increased signal in the PAT images with SWNTs compared to blood (both figures are shown in the same range of colorbar). Figures 4(g) and 4 (h) compare the image profiles along the horizontal and vertical lines (along the dotted lines in Figs. 4(e) and 4(f)), respectively. Compared to blood, SWNTs showed a ~6.3 fold signal improvement along the horizontal line and a ~5.6 fold signal improvement along the vertical line (normalized to blood). These results are consistent with the PA data presented in figure 3. The variation in the signal improvement along the horizontal and vertical directions for both TAT and PAT is possibly due to the anisotropic spatial resolution.

Figures 4(i) and 4(j) show the reconstructed tissue-mimicking phantom TAT images for DI water and SWNTs, respectively. The dark spot on the image, marked with a solid arrow, is a needle used to hold the tissue sample. The boundary of the fat tissue is marked with a dashed arrow. The images clearly show greater contrast for the SWNTs-filled vial than for the DI water-filled vial. Figures 4(k) and 4(l) show PAT images with blood and SWNTs, respectively, for the tissue phantom. The results are similar to those obtained by TAT imaging: the SWNTs sample displays greater contrast than blood.

The main motivation in this study was to show that SWNTs can themselves generate both TA and PA signals. Towards this end, as discussed above, a non-ionic, nearly neutral SWNT solution was used for the phantom imaging since, in the future, *in vivo* imaging studies will be carried out by injecting SWNTs in solution (most probably in a buffer solution with water as its main component) instead of solid SWNT powder. Our results show that SWNTs could be used for TA/PA imaging, as the intrinsic absorption properties of SWNTs are able to produce equivalent or stronger (depending on the SWNTs concentrations) TA/PA signals than a known endogenous absorber (more than water in the case of TAT, and more than blood in the case of PAT). Additionally, a substantial enhancement in the PA signal was measured *in vitro* when the SWNTs were mixed with blood. Thus, we conclude that when the SWNT solution is mixed with water/blood, it enhances the total TA/PA signal from the water/blood. Furthermore, TA/PA signals generated by SWNTs could be used for imaging applications where there are no endogenous signals. For example, using PA imaging and SWNTs, we have carried out *in vivo* sentinel lymph node mapping non-invasively.[36] In this application, there was no blood signal involved, and the PA signals generated by the SWNTs were used for imaging the sentinel lymph nodes. Another example is a targeted molecular imaging application where the TA/PA signal would be generated from the contrast agents themselves.

As shown in previous studies,[37] the optical absorption properties of SWNTs are strong in the visible and NIR region. Currently, no studies have demonstrated SWNTs' absorption property in the 3 GHz microwave region, but their conductive properties make them promising for strong absorption.[38] SWNTs have high permittivity when exposed to electromagnetic radiation at frequencies between 0.5 GHz to 3 GHz, and as the frequency increases above 3 GHz, the permittivity decreases,[39,40] indicating that SWNTs could be used as contrast agents below 3 GHz. Another study showed the feasibility of iron oxide nanoparticles as a contrast agent in TAT.[41] To the best of our knowledge, this is the first study that explores the efficacy of SWNTs as contrast agents for multi-modal imaging with TAT/PAT. This study successfully demonstrates that SWNTs are suitable as a contrast agent for both TAT and PAT. The SWNTs also allow contrast-enhanced deep tissue imaging with TAT. In this study, for TAT, we observed contrast enhancement due to the SWNTs at an rf frequency of 3 GHz. It will be particularly interesting to characterize their effectiveness at lower rf frequencies. It is well known that the human body becomes more transparent at lower rf frequencies, allowing an increase in the imaging depth. However, due to lower tissue absorbance at lower rf frequencies, the intrinsic image contrast suffers. Therefore, if the SWNTs work as a contrast agent at lower rf frequencies, we can potentially achieve low-background, high-sensitivity, deep tissue imaging.

The broad absorption range of SWNTs in the visible/NIR region[37] is also beneficial for optical imaging as one can use a wide range of laser wavelengths for imaging without the need to tune the contrast agent to a particular wavelength to optimize light absorption. In comparison, other contrast agents suitable for PAT, such as gold nanoparticles, are tuned to a particular wavelength range and can be used only with light within that range.[17,42] Furthermore, our results suggest that a minimum detectable concentration of SWNTs should be comparable to that of gold nanoparticles.[42] Using previously derived equations,[43] we have calculated that carbon nanotubes of 2 nm average diameter and 1 μm average length have ~10^5 carbon atoms, giving an average molecular weight of ~10^6 Da or g/mol (multiply the number of carbon atoms by 12, the atomic weight of carbon). From figure 3, it is clear that the minimum detectable concentration is less than 0.1 mg/ml or 100 nM (0.1 mg/ml/10^6 g/mol) SWNTs concentration, allowing their detection in the nM range. It is also evident that even at 0.1 mg/ml SWNTs concentration, there is a 35% increase in peak-to-peak TA signal compared to DI water and a 32% increase in peak-to-peak PA signal compared to blood. For targeted molecular imaging applications, an important consideration is not only the enhancement, but also the signal generated by the SWNTs themselves. In this study, we have detected signals with very high

signal-to-noise ratio (SNR > 100 in both TA and PA) at 1 mg/ml SWNT concentration, suggesting that the minimum detectable SWNT concentration could be as low as 0.01 mg/ml or ~ 10 nM with this system, making them suitable for *in vivo* applications in various tissues. In general, the minimum detectable concentration of an exogenous contrast agent by PAT/TAT is dependent on many factors, such as incident light/microwave energy, ultrasound detector sensitivity, data acquisition electronics etc. For our future *in vivo* studies, the concentration(s) of the SWNTs will depend on the specific application and the sensitivity of the imaging system.[36,44]

The SWNTs also have a number of additional benefits. (1) Other than TAT and PAT, SWNTs can also be used as a contrast agent for other imaging modalities such as MRI, PET, NIR optical imaging, and nuclear imaging.[22–25] Therefore, in a true sense they can work as a multi-modal contrast agent. (2) The external carbon sheath of the SWNTs can be directly functionalized for targeting and drug delivery. This capability is not possible for other optical contrast agents such as gold nanoparticles, where one does not functionalize the gold, but rather the capping agents or the biocompatible coating used to stabilize and/or dispense gold nanoparticles in solution. (3) SWNTs now offer the exciting and tantalizing prospect of achieving TAT and/or PAT molecular imaging and simultaneous therapy by NIR and rf-induced hyperthermia. Recently, SWNTs have been shown to facilitate the NIR and rf-induced ablation of tumor cells/tissues.[25,45] Thus, these unique features of SWNTs should allow the design of multi-modal imaging and multi-therapeutic approaches within a single platform.

Conclusions

In summary, we have successfully shown that SWNTs provide more than two fold signal enhancement in TAT at 3 GHz and more than six fold signal enhancement in PAT at 1064 nm. These results indicate that by using SWNTs as contrast agents, the functional information from TAT and PAT together with other structural imaging modalities will be advantageous for early cancer diagnosis. At lower radio frequencies, these exogenous contrast agents offer a new paradigm for low-background, high-sensitivity, deep-tissue, and targeted molecular imaging by TAT.

Acknowledgments

This work was sponsored by National Institutes of Health grants R01 EB000712, R01 NS46214 (Bioengineering Research Partnerships), R01 EB008085, and U54 CA136398 (Network for Translational Research) (LV) and the Office of the Vice President of Research at Stony Brook University, Carol M. Baldwin fund (SB). L.W. has a financial interest in Endra, Inc., which, however, did not support this work. The authors would like to thank Dr. Oleg Gang and Dr. Huming Xiong at the Center for Functional Nanomaterials, Brookhaven National Laboratory for access to the AFM, Mr. Tom Salagaj and Mr. Christopher Jensen at FirstNano/CVD Equipment Corporation for access to their CVD facilities and Dr. Eunah Lee at Horiba JvonYvon, Edison, NJ for the Raman Spectroscopy measurements.

References

1. Ottobrini L, Ciana P, Biserni A, Lucignani G, Maggi A. Molecular imaging: A new way to study molecular processes in vivo. Molecular and Cellular Endocrinology 2006;246(1–2):69–75. [PubMed: 16388894]
2. Ntziachristos V, Ripoll J, Wang LHV, Weissleder R. Looking and listening to light: the evolution of whole-body photonic imaging. Nature Biotechnology 2005;23(3):313–320.
3. Meikle SR, Kench P, Kassiou M, Banati RB. Small animal SPECT and its place in the matrix of molecular imaging technologies. Physics in Medicine and Biology 2005;50(22):R45–R61. [PubMed: 16264248]
4. Frangioni JV. In vivo near-infrared fluorescence imaging. Current Opinion in Chemical Biology 2003;7(5):626–634. [PubMed: 14580568]

5. Krause, W. Contrast agents II: Optical, Ultrasound, X-Ray Imaging and Radiopharmaceutical Imaging. Springer; 2002.
6. Ritman EL. Molecular imaging in small animals – Roles for micro-CT. Journal of Cellular Biochemistry 2002:116–124. [PubMed: 12552611]
7. Wang LHV, Zhao XM, Sun HT, Ku G. Microwave-induced acoustic imaging of biological tissues. Review of Scientific Instruments 1999;70(9):3744–3748.
8. Ku G, Fornage BD, Jin X, Xu MH, Hunt KK, Wang LHV. Thermoacoustic and photoacoustic tomography of thick biological tissues toward breast imaging. Technology in Cancer Research & Treatment 2005;4(5):559–565. [PubMed: 16173826]
9. Wang XD, Pang YJ, Ku G, Xie XY, Stoica G, Wang LHV. Noninvasive laser-induced photoacoustic tomography for structural and functional in vivo imaging of the brain. Nature Biotechnology 2003;21 (7):803–806.
10. Ku G, Wang XD, Xie XY, Stoica G, Wang LHV. Imaging of tumor angiogenesis in rat brains in vivo by photoacoustic tomography. Applied Optics 2005;44(5):770–775. [PubMed: 15751858]
11. Li ML, Oh JT, Xie XY, Ku G, Wang W, Li C, Lungu G, Stoica G, Wang LHV. Simultaneous molecular and hypoxia imaging of brain tumors in vivo using spectroscopic photoacoustic tomography. Proceedings of the IEEE 2008;96(3):481–489.
12. Pramanik M, Ku G, Li CH, Wang LHV. Design and evaluation of a novel breast cancer detection system combining both thermoacoustic (TA) and photoacoustic (PA) tomography. Medical Physics 2008;35(6):2218–2223. [PubMed: 18649451]
13. Kruger RA, Miller KD, Reynolds HE, Kiser WL, Reinecke DR, Kruger GA. Breast cancer in vivo: Contrast enhancement with thermoacoustic CT at 434 MHz – Feasibility study. Radiology 2000;216 (1):279–283. [PubMed: 10887262]
14. Kruger RA, Reinecke DR, Kruger GA. Thermoacoustic computed tomography-technical considerations. Medical Physics 1999;26(9):1832–1837. [PubMed: 10505871]
15. Oraevsky, AA.; Savateeva, EV.; Solomatin, SV.; Karabutov, AA.; Andreev, VG.; Gatalica, Z.; Khamapirad, T.; Henrichs, PM. Optoacoustic Imaging of Blood for Visualization and Diagnostics of Breast Cancer. In: Oraevsky, AA., editor. Biomedical Optoacoustics III. Vol. 4618. 2002. p. 81-94.
16. Xu MH, Wang LHV. Photoacoustic imaging in biomedicine. Review of Scientific Instruments 2006;77(4):041101.
17. Wang YW, Xie XY, Wang XD, Ku G, Gill KL, O'Neal DP, Stoica G, Wang LHV. Photoacoustic tomography of a nanoshell contrast agent in the in vivo rat brain. Nano Letters 2004;4(9):1689–1692.
18. Wang XD, Xie XY, Ku GN, Wang LHV. Noninvasive imaging of hemoglobin concentration and oxygenation in the rat brain using high-resolution photoacoustic tomography. Journal of Biomedical Optics 2006;11(2):024015. [PubMed: 16674205]
19. Lungu GF, Li ML, Xie XY, Wang LHV, Stoica G. In vivo imaging and characterization of hypoxia-induced neovascularization and tumor invasion. International Journal of Oncology 2007;30(1):45–54. [PubMed: 17143511]
20. Schneider BP, Miller KD. Angiogenesis of breast cancer. Journal of Clinical Oncology 2005;23(8): 1782–1790. [PubMed: 15755986]
21. Vaupel P, Mayer A, Briest S, Hockel M. Hypoxia in breast cancer: Role of blood flow, oxygen diffusion distances, and anemia in the development of oxygen depletion. Oxygen Transport to Tissue XXVI 2005;566:333–342.
22. Sitharaman B, Kissell KR, Hartman KB, Tran LA, Baikalov A, Rusakova I, Sun Y, Khant HA, Ludtke SJ, Chiu W, Laus S, Toth E, Helm L, Merbach AE, Wilson LJ. Superparamagnetic gadonanotubes are high-performance MRI contrast agents. Chemical Communications 2005;(31):3915–3917. [PubMed: 16075070]
23. McDevitt MR, Chattopadhyay D, Kappel BJ, Jaggi JS, Schiffman SR, Antczak C, Njardarson JT, Brentjens R, Scheinberg DA. Tumor targeting with antibody-functionalized, radiolabeled carbon nanotubes. Journal of Nuclear Medicine 2007;48(7):1180–1189. [PubMed: 17607040]
24. Liu Z, Cai WB, He LN, Nakayama N, Chen K, Sun XM, Chen XY, Dai HJ. In vivo biodistribution and highly efficient tumour targeting of carbon nanotubes in mice. Nature Nanotechnology 2007;2 (1):47–52.

25. Cherukuri P, Gannon CJ, Leeuw TK, Schmidt HK, Smalley RE, Curley SA, Weisman RB. Mammalian pharmacokinetics of carbon nanotubes using intrinsic near-infrared fluorescence. Proceedings of the National Academy of Sciences of the United States of America 2006;103(50): 18882–18886. [PubMed: 17135351]
26. Hughes ME, Brandin E, Golovchenko JA. Optical absorption of DNA-carbon nanotube structures. Nano Letters 2007;7(5):1191–1194. [PubMed: 17419658]
27. Berciaud S, Cognet L, Poulin P, Weisman RB, Lounis B. Absorption spectroscopy of individual single-walled carbon nanotubes. Nano Letters 2007;7(5):1203–1207. [PubMed: 17385932]
28. Gannon CJ, Cherukuri P, Yakobson BI, Cognet L, Kanzius JS, Kittrell C, Weisman RB, Pasquali M, Schmidt HK, Smalley RE, Curley SA. Carbon nanotube-enhanced thermal destruction of cancer cells in a noninvasive radiofrequency field. Cancer 2007;110(12):2654–2665. [PubMed: 17960610]
29. IEEE standard for safety levels with respect to human exposure to radio frequency electromagnetic fields 3 kHz to 300 GHz, IEEE Std C95.1, 1999 Edition.
30. Laser Institute of America, American National Standard for Safe Use of Lasers ANSI Z136.1–2000 (American National Standards Institute, Inc., New York, NY, 2000).
31. Song KH, Wang LHV. Deep reflection-mode photoacoustic imaging of biological tissue. Journal of Biomedical Optics 2007;12(6):060503. [PubMed: 18163798]
32. Fu Q, Huang SM, Liu J. Chemical vapor depositions of single-walled carbon nanotubes catalyzed by uniform Fe2O3 nanoclusters synthesized using diblock copolymer micelles. Journal of Physical Chemistry B 2004;108(20):6124–6129.
33. Dresselhaus MS, Dresselhaus G, Saito R, Jorio A. Raman spectroscopy of carbon nanotubes. Physics Reports-Review Section of Physics Letters 2005;409(2):47–99.
34. White B, Banerjee S, O'Brien S, Turro NJ, Herman IP. Zeta-potential measurements of surfactant-wrapped individual single-walled carbon nanotubes. Journal of Physical Chemistry C 2007;111(37): 13684–13690.
35. Chaudhary SS, Mishra RK, Swarup A, Thomas JM. Dielectric-Properties of Normal and Malignant Human-Breast Tissues at Radiowave and Microwave-Frequencies. Indian Journal of Biochemistry & Biophysics 1984;21(1):76–79.
36. Pramanik M, Song KH, Swierczewska M, Green D, Sitharaman B, Wang LHV. *In vivo* carbon nanotube-enhanced non-invasive photoacoustic mapping of the sentinel lymph node. Physics in Medicine and Biology. 2009under review
37. O'Connell MJ, Bachilo SM, Huffman CB, Moore VC, Strano MS, Haroz EH, Rialon KL, Boul PJ, Noon WH, Kittrell C, Ma JP, Hauge RH, Weisman RB, Smalley RE. Band gap fluorescence from individual single-walled carbon nanotubes. Science 2002;297(5581):593–596. [PubMed: 12142535]
38. Saib A, Bednarz L, Daussin R, Bailly C, Lou X, Thomassin JM, Pagnoulle C, Detrembleur C, Jerome R, Huynen I. Carbon nanotube composites for broadband microwave absorbing materials. IEEE Transactions on Microwave Theory and Techniques 2006;54(6):2745–2754.
39. Grimes CA, Mungle C, Kouzoudis D, Fang S, Eklund PC. The 500 MHz to 5.50 GHz complex permittivity spectra of single-wall carbon nanotube-loaded polymer composites. Chemical Physics Letters 2000;319(5–6):460–464.
40. Watts PCP, Hsu WK, Barnes A, Chambers B. High permittivity from defective multiwalled carbon nanotubes in the X-band. Advanced Materials 2003;15(7–8):600–603.
41. Jin X, Keho A, Meissner K, Wang LHV. Iron-oxide nanoparticles as a contrast agent in thermoacoustic tomography. Proc SPIE 2007:6437.
42. Eghtedari M, Oraevsky A, Copland JA, Kotov NA, Conjusteau A, Motamedi M. High sensitivity of in vivo detection of gold nanorods using a laser optoacoustic imaging system. Nano Letters 2007;7 (7):1914–1918. [PubMed: 17570730]
43. Yamamoto K, Kamimura T, Matsumoto K. Nitrogen doping of single-walled carbon nanotube by using mass-separated low-energy ion beams. Japanese Journal of Applied Physics Part 1-Regular Papers Short Notes & Review Papers 2005;44(4A):1611–1614.
44. De La Zerda A, Zavaleta C, Keren S, Vaithilingam S, Bodapati S, Liu Z, Levi J, Smith BR, Ma TJ, Oralkan O, Cheng Z, Chen XY, Dai HJ, Khuri-Yakub BT, Gambhir SS. Carbon nanotubes as photoacoustic molecular imaging agents in living mice. Nature Nanotechnology 2008;3(9):557–562.

45. Kam NWS, O'Connell M, Wisdom JA, Dai HJ. Carbon nanotubes as multifunctional biological transporters and near-infrared agents for selective cancer cell destruction. Proceedings of the National Academy of Sciences of the United States of America 2005;102(33):11600–11605. [PubMed: 16087878]

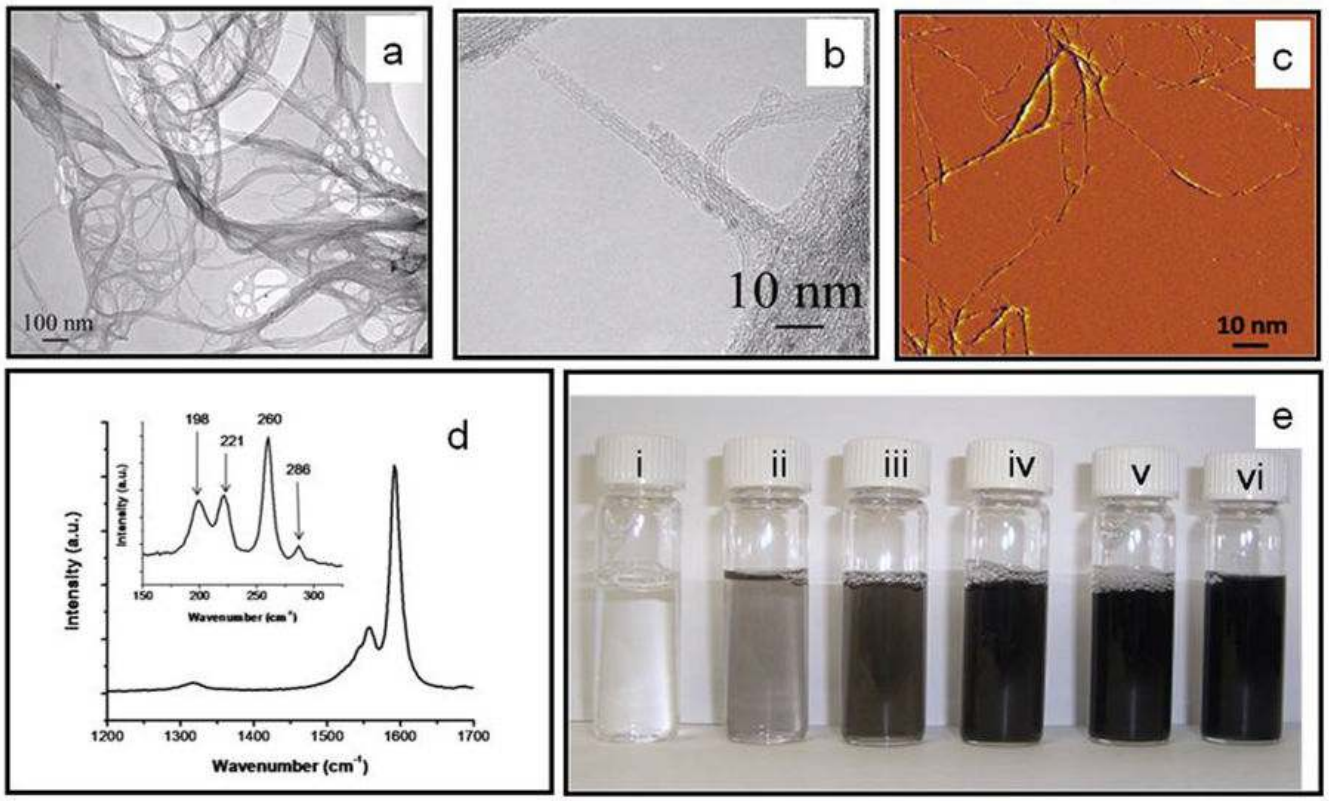

FIG. 1.

(a) A low resolution bright field TEM, (b) HRTEM image of bundled SWNTs grown using Fe as the catalyst. (c) Tapping mode AFM images of dispersed SWNTs. (d) D-band and G-band Raman spectra of the SWNTs. The inset shows the radial breathing modes. (e) Vials contain aqueous dispersions of SWNTs in Pluronic® F127 after being sonicated. From left to right the concentrations are i) 0 mg/ml, ii) 0.1 mg/ml, iii) 0.25 mg/ml, iv) 0.5 mg/ml, v) 0.75 mg/ml and, vi) 1 mg/ml.

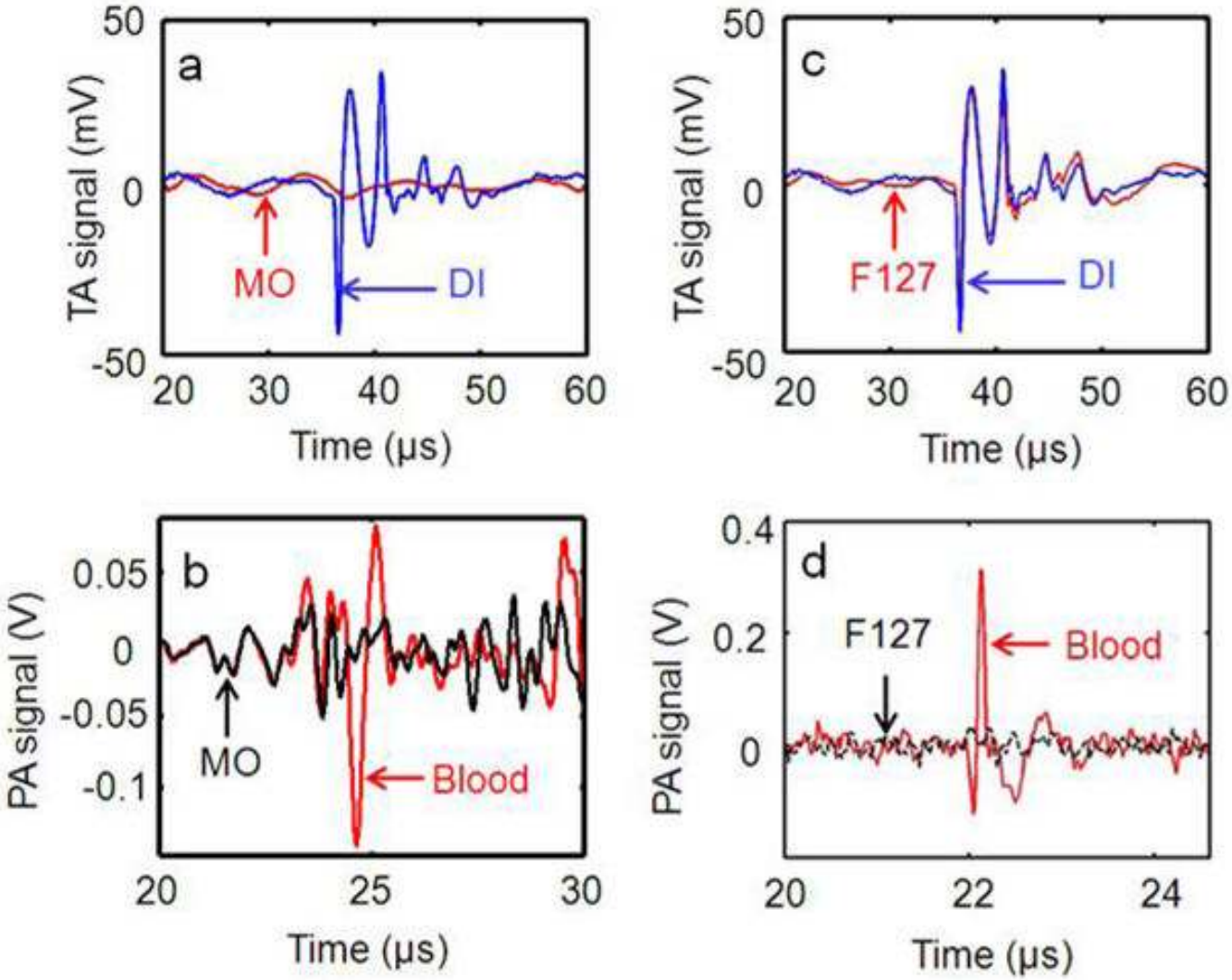

FIG. 2.

(a) TA signals from a LDPE vial (I.D. 6 mm, volume 1 cc) filled with mineral oil (MO) and De-ionized water (DI). (b) PA signals from LDPE vial filled with blood and mineral oil (MO) at 1064 nm. (c) TA signals from the LDPE vial filled with 1% Pluronic® F127 solution (F127) and De-ionized water (DI). (d) PA signals from a tube (Silastic® laboratory tubing, Dow Corning Corp., with I.D. 300 μm, O.D. 640 μm) filled with blood and with 1% Pluronic® F127 solution (F127).

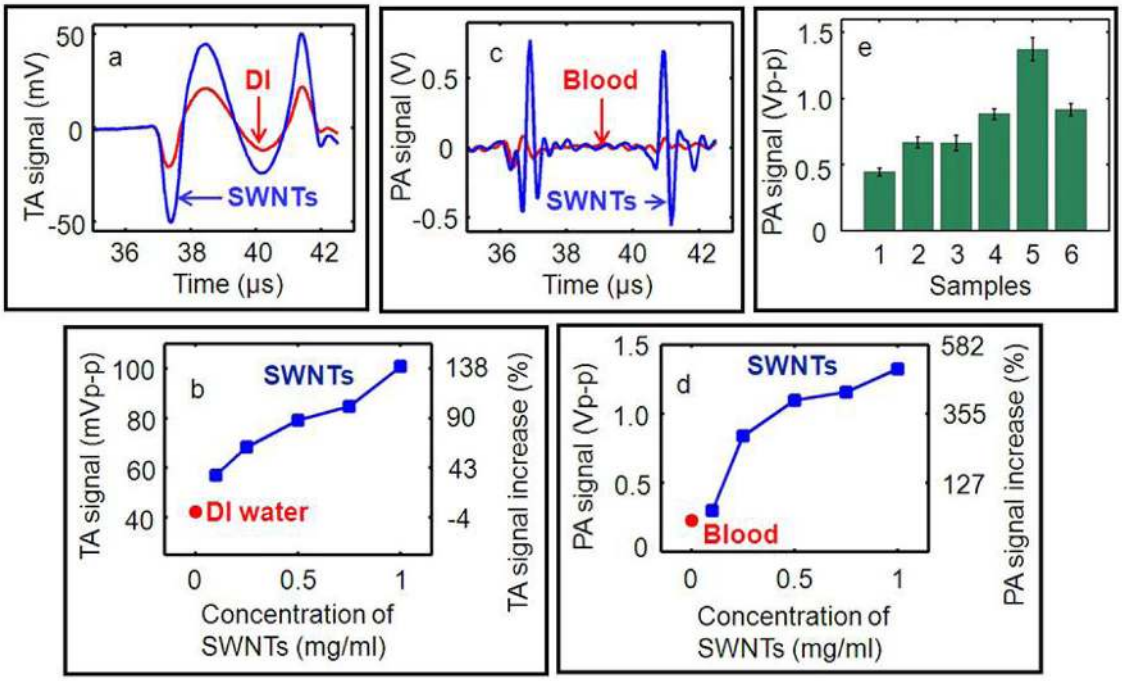

FIG. 3.

(a) TA signals at 3 GHz from a LDPE vial (I.D. 6 mm, volume 1 cc) filled with DI water and 1 mg/ml SWNTs. (b) Peak-to-peak TA signal amplitude and fractional increase in TA signal versus SWNTs concentration. (c) PA signals at 1064 nm wavelength from a LDPE vial filled with rat blood and 1 mg/ml SWNTs. (d) Peak-to-peak PA signal amplitude and fractional increase in PA signal versus SWNTs concentration. (e) Peak-to-peak PA signal amplitudes from blood mixed with various amounts of SWNTs. 1: Blood only, 2: blood (90% v/v) + SWNTs (10% v/v), 3: blood (75% v/v) + SWNTs (25% v/v), 4: blood (50% v/v) + SWNTs (50% v/v), 5: blood (25% v/v) + SWNTs (75% v/v), and 6: SWNTs alone. The light source was of 754 nm wavelength. A tube (Silastic® laboratory tubing, Dow Corning Corp., with I.D. 300 μm, O.D. 640 μm) was used to hold the sample.

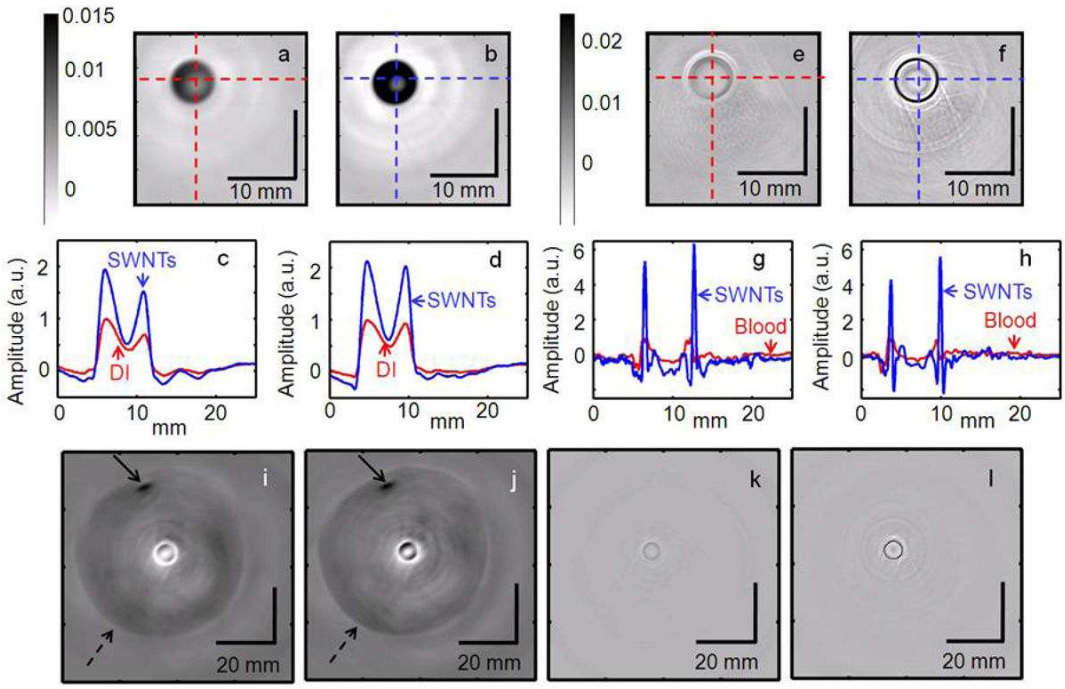

FIG. 4.

(a) Cross sectional TAT image of the vial (LDPE, I.D. 6mm, 1 cc volume) containing DI water. (b) Cross sectional TAT image of the vial containing 1 mg/ml SWNTs. (c) Comparison of the signal profiles along the horizontal lines across the centers of the vials in (a) and (b). (d) Comparison of the signal profiles along the vertical lines across the centers of the vials in (a) and (b). (e) Cross sectional PAT image of the vial containing blood. (f) Cross sectional PAT image of the vial containing 1 mg/ml SWNTs. (g) Comparison of the signal profiles along the horizontal lines across the centers of the vials in (e) and (f). (h) Comparison of the signal profiles along the vertical lines across the centers of the vials in (e) and (f). (i) Cross sectional TAT image of the vial containing DI water inside pork fat tissue. (j) Cross sectional TAT image of the vial containing 1 mg/ml SWNTs inside pork fat tissue. The solid arrow points to the needle used to hold the fat tissue, and the dashed arrow indicates the boundary of the fat tissue. (k) Cross sectional PAT image of the blood vial inside pork fat tissue. (l) Cross sectional PAT image of the 1 mg/ml SWNTs vial inside pork fat tissue.

Table 1

Peak-to-peak TA/PA signal amplitudes obtained from various samples. A LDPE (6 mm I.D., 1 cc volume) vial was the sample holder. TA was done at 3 GHz and PA was done at 1064 nm wavelength.

Sample	Peak-to-peak TA signal amplitude (mV)		Peak-to-peak PA signal amplitude (mV)	
	0.5″ active area transducer	**0.25″ active area transducer**	**0.5″ active area transducer**	**0.25″ active area transducer**
Deionized water	47	14	—	—
Single-walled carbon nanotube (1 mg/ml)	**95**	**28**	**113**	**81**
Fullerene (C_{60})	51	15	55	68
Graphite microparticles	38	10	28	30
Multi-walled carbon nanotube (OD = 10–15 nm)	40	12	95	81
Aldrich multi-walled carbon nanotube (OD = 20–30 nm)	40	12	58	67
Multi-walled carbon nanotube (OD = 40–70 nm)	39	10	28	27
Multi-walled carbon nanotube (OD = 110–170 nm)	47	15	62	70
Blood	—	—	33	31